Effects of nonsphericity on mineral dust modeling

Paul Ginoux

Goddard Earth Sciences and Technology, University of Maryland Baltimore County, Catonsville, Maryland, USA

Received 8 May 2002; revised 16 September 2002; accepted 14 November 2002; published 23 January 2003.

[1] The dependency of nonsphericity on gravitational settling of mineral dust particles is parameterized for prolate ellipsoids and Reynolds number lower than 2. The settling speed is numerically solved from the momentum equation as a function of particle diameter and aspect ratio. The reduction of settling speed due to nonsphericity is included in the Global Ozone Chemistry Aerosol Radiation and Transport (GOCART) model to simulate dust size distribution for April 2001. Two numerical schemes for solving sedimentation are compared. For particles of diameter greater than 5 μm, the simulated size distribution is sensitive to the numerical sedimentation scheme. Changing the particle shape from spherical to nonspherical with $\lambda = 2$ makes little difference to the simulated surface concentration and size distribution except at the periphery of the dust sources. However, when very elongated particles ($\lambda = 5$) are simulated, the differences between nonspherical and spherical particles are significant. With limited in situ measurements reporting most frequent λ around 1.5, the overall effects on global modeling is rather negligible and the essential benefit is to relax the CFL condition of Eulerian settling schemes. *INDEX TERMS:* 0305 Atmospheric Composition and Structure: Aerosols and particles (0345, 4801); 0368 Atmospheric Composition and Structure: Troposphere—constituent transport and chemistry; 3210 Mathematical Geophysics: Modeling; *KEYWORDS:* dust, settling, sedimentation, nonsphericity, global model

Citation: Ginoux, P., Effects of nonsphericity on mineral dust modeling, *J. Geophys. Res.*, *108*(D2), 4052, doi:10.1029/2002JD002516, 2003.

1. Introduction

[2] Due to their optical properties, dust particles could play an important role on the radiation energy balance and climate forcing [*Tegen et al.*, 1996; *Sokolik and Toon*, 1996; *Weaver et al.*, 2002]. Several studies have shown that nonsphericity significantly affects the optical properties, and in particular the phase function [e.g., *Mischenko*, 1991; *Mischenko and Travis*, 1994; *Mischenko et al.*, 1995; *Koepke and Hess*, 1988; *Schulz et al.*, 1999; *Kalashnikova and Sokolik*, 2002]. From a mechanical point of view, the effect of nonsphericity on particles sedimentation have been studied for the past several decades, with applications in multiphases fluid flow [e.g., *Boothroyd*, 1971], cloud ice crystals [*Turco et al.*, 1982], and particles in Titan's atmosphere [*Toon et al.*, 1980]. However, current global transport models of mineral dust aerosol assume spherical particles. The motivation for this assumption is that optically, at the global scale, the most important particles are submicrometers. For such small particles sedimentation is a negligible removal process compare to wet deposition. However, at a regional scale, near the dust sources, the radiative effect of larger particles is not negligible.

[3] Considering spherical particles, models have been able to reproduce the observed size distribution up to 10 μm. Beyond that diameter, models generally underestimate dust loading [*Tegen and Fung*, 1994; *Ginoux et al.*, 2001; *Colarco et al.*, 2002]. Different explanations have been proposed but none have considered the effect of nonsphericity. The objective of this paper is to reexamine the assumption of sphericity in light of measured dust shape, and to evaluate the impact of nonsphericity on dust distribution. Another motivation of this study is to eventually find a physical explanation for the observed long-range transport of giant particles. For example, *Goudie and Middleton* [2001] reported that particles larger than 62.5 μm are commonly carried from Sahara to the British Isles.

[4] In the first section, the momentum equation is established for nonspherical particles with Reynolds number lower than 2. The equation is nonlinear in terms of the settling speed. A new approximation, taking into account the particle radius and shape, is presented. In the second section, the measured shape and aspect ratio of dust particles are summarized. In the third section, different values of aspect ratio are implemented in the treatment of gravitational settling in a global transport model. The results of simulations between spherical and nonspherical particles are compared. The effects of nonsphericity on dust mass loading, size distribution and surface concentration are analyzed. Finally, the importance and utility of the implementation of nonspherical particles in transport model will be discussed.

2. Measurements of Particles Shape

[5] There are very few measurements of particle shapes from air sampling. *Okada et al.* [2001] have determined the

0148-0227/03/2002JD002516$09.00

Table 1. Shape Property, Size, and Thickness of Dust Minerals, as Reported by *Grim* [1968]

Mineral	Property	Diameter	Thickness
Kaolinite	Flake-shaped with prominent elongation in one direction	0.3–4 μm	0.05–2 μm
Halloysite	Like kaolinite but tubular instead of flake		
Smectite	extremely small	300 Å	50–80 Å
Illite	Irregular aggregates	0.1–10 μm	30 Å
Chlorite	similar to Illite		
Palygorskite	Elongate lath-shaped	>1 μm	50–100 Å

aspect ratio distribution of dust collected in China. They screened their samples to analyze the shape of particles with size ranging from 0.2 to 4 μm diameter. They found that most of the particles in that size range can be considered as ellipsoid characterized by an aspect ratio (λ) greater than 1. Their frequency distribution of aspect ratio is very similar to the one measured by *Krotkov et al.* [1999] for volcanic ash particles. The maximum frequency is for $\lambda \sim 1.5$, and the highest value of λ is around 5. *Okada et al.* [2001] noted that particles larger than 4 μm have more complex shape and did not provide characteristic λ values. Most particles with diameter less than 50 μm are clay or silt minerals. *Glaccum and Prospero* [1980] have measured the mineralogy of Saharan dust collected at Cape Verde. Their analysis indicated that the most frequent minerals are in decreasing order: illite (∼50%), quartz (10–20%), calcite, kaolinite, plagioclase, chlorite, and montmorillonite. *Caquineau et al.* [1998] have also measured dust mineralogy at Sal Island and showed large variations in mineralogy depending of the source areas. Electron microscopy can provide information on the shape properties. *Grim* [1968] reported characteristic values of diameter and thickness of several minerals from different studies using electron microscopy. The data are summarized in Table 1. It appears from this table that the ratio between length and width of elongated minerals can be as high as 10.

3. Settling Velocity of Prolate Ellipsoid

3.1. Previous Formulations

[6] Formulations of settling speed as a function of shape have been established in the past for the atmosphere. *Fuchs* [1964] provided a detail analysis of fall speed of ellipsoids and cylinders for different elongations. However, he did not consider explicitly the nonlinear dependency of the fall speed for large Reynolds number. For Reynolds number less than 0.1, the nonlinearity is negligible and the Stokes law can be applied, but for larger Reynolds number such nonlinearity cannot be neglected. To solve the problem, *Fuchs* [1964] does not explicitly solve the equation but proposed an empirical formula. With actual computers, solving nonlinear equation is no more an issue. *Turco et al.* [1982] have established formula of fall speeds for mesospheric ice crystals. They considered cubic, hexagonal and cylindrical shapes for particle sizes ranging from 10 Å to 2.6 μm. Their formulations are established for particles at high altitude where fall speed depends linearly on the particle radius.

3.2. Settling Speed for Prolate Ellipsoid

[7] A particle of mass m_p settling at a velocity $\mathbf{u}$ in a fluid is subjected to the gravitational force $m_p\mathbf{g}$ and the drag force $\mathbf{F}_{drag}$. The momentum equation can be expressed in the vertical by:

$$m_p \frac{du}{dt} = m_p g + F_{drag} \tag{1}$$

where u, g, and F_{drag} are the vertical components of the velocity, the acceleration of gravity, and the drag force, respectively. At steady state, the settling particle reaches a terminal settling speed u_∞ and (1) is simplified to $F_{drag} = -m_p g$. The drag force is generally expressed in terms of an empirical drag coefficient C_D such that

$$F_{drag} = \frac{1}{2} C_D A_p \rho u_\infty^2, \tag{2}$$

where A_p is the projected area of the body normal to the flow, ρ is the fluid density. Dimensional analysis shows that the drag coefficient is correlated to the Reynolds number, Re. For a particle of diameter D_p settling at a speed u_∞ in a fluid of density ρ and dynamic viscosity μ, the Reynolds number for the particle is given by $Re = R_e = \frac{\rho u_\infty D_p}{\mu}$. For spherical particles with $D_p < 100$ μm, C_D can be calculated, by the following correlation [*Seinfeld and Pandis*, 1998]:

$$C_D = \frac{24}{Re}\left[1 + \frac{3}{16}Re + \frac{9}{160}Re^2 \ln(2Re)\right] \quad Re < 2 \tag{3}$$

For nonspherical particles, *Boothroyd* [1971] has established a correlation depending also on a sphericity factor Φ_p, and given by

$$C_D = \frac{24}{Re}\left[1 + \frac{3}{16}Re + \frac{9}{160}Re^2 \ln(2Re) + \frac{10(1-\Phi_p)}{\Phi_p}Re^{0.35}\right] \quad Re < 2 \tag{4}$$

where the sphericity factor Φ_p is the surface area of equivalent volume divided by the particle surface area (S_p) and is given by the formula:

$$\Phi_p = \frac{\pi\left(\frac{6V_p}{\pi}\right)^{2/3}}{S_p} \tag{5}$$

where V_p and S_p are the particle volume and surface area, respectively. The drag coefficient decreases with increasing Reynolds number but for nonspherical particles the decrease is less pronounced. For example, with $Re = 0.1$ (or $D_p \sim 20$ μm in a standard atmosphere), the drag coefficient increases by a factor 2.5 from spherical ($\Phi_p = 1$) to elongated particles ($\Phi_p = 0.1$).

[8] In the axes (X, Y, Z), prolate ellipsoid is defined by the equation,

$$\frac{X^2}{a^2}+\frac{Y^2}{b^2}+\frac{Z^2}{b^2}=1 \quad a>b, \tag{6}$$

and its aspect ratio $\lambda=\frac{a}{b}>1$. The volume V_p and the surface area S_p of this ellipsoid are given by

$$\begin{aligned} V_p &= \frac{4}{3}\pi ab^2 \\ S_p &= 2\pi b^2 + 2\pi ab\frac{\arcsin e}{e}, \end{aligned} \tag{7}$$

with $e=\frac{\sqrt{a^2-b^2}}{a}$

[9] The sphericity factor expressed in terms of λ is given by

$$\Phi_p=\frac{2\lambda^{2/3}}{1+\frac{\lambda^2}{\sqrt{\lambda^2-1}}\arcsin\left(\sqrt{1-\frac{1}{\lambda^2}}\right)} \tag{8}$$

[10] The projected area A_p will depend on the orientation of the main axis of the ellipsoid relative to the vertical. Theoretically, particles settling at terminal speed u_∞ maintain a preferential orientation [*Kagermann and Khler*, 1982]. The orientation will depend on the initial conditions, the inertia of the particle and the environmental conditions. Considering the macroscopic scale of transport models, it is reasonable to assume that the ensemble of particles will be randomly oriented. If we consider a rotation θ in the plane (X, Z), the projected ellipse in the horizontal plane has a width b and a length $a_{proj}=a^2\cos^2\theta+b^2\sin^2\theta$. For randomly oriented particles, A_p is replaced by the spherically averaged value $\hat{A}_p$ given by

$$\hat{A}_p=\frac{4\int_0^{\pi/2}\pi b a_{proj}d\theta}{4\int_0^{\pi/2}d\theta}=2baE(e), \tag{9}$$

where $E(e)$ is the complete elliptic integral of the second kind and $0<e=\frac{\sqrt{a^2-b^2}}{a}=\frac{\sqrt{\lambda^2-1}}{\lambda}<1$.

[11] Finally, the equivalent diameter D_p is expressed as a function of λ,

$$\begin{aligned} D_p &= 2\left(\frac{S_p}{\pi}\right)^{1/2} \\ &= b\left(2+2\frac{\lambda^2}{\sqrt{1-\lambda^2}}\arcsin\sqrt{1-\frac{1}{\lambda^2}}\right)^{1/2} \\ &= b\Psi_D(\lambda) \end{aligned} \tag{10}$$

[12] By replacing each terms in (1) by their expression in λ, we obtain the following expressions for u_∞,

$$\begin{aligned} &\left[1+\frac{3}{16}\left(\frac{\rho u_\infty D_p(\lambda)}{\mu}\right)+\frac{9}{160}\left(\frac{\rho u_\infty D_p(\lambda)}{\mu}\right)^2\ln\left(2\frac{\rho u_\infty D_p(\lambda)}{\mu}\right)\right. \\ &\quad\left.+\frac{10\left(1-\Phi_p(\lambda)\right)}{\Phi_p(\lambda)}\left(\frac{\rho u_\infty D_p(\lambda)}{\mu}\right)^{0.35}\right]u_\infty \\ &\quad=\frac{1}{18}\frac{\left(\rho_p-rho\right)D_p(\lambda)^2 g}{\mu}\left(\frac{\pi}{E(\lambda)\psi_D(\lambda)}\right) \quad Re<2 \end{aligned} \tag{11}$$

This equation is nonlinear in u_∞, and $E(\lambda)$ has no analytical solution. It has to be resolved numerically. As λ increases, the terms E and Φ_p decrease while Ψ_D increases. For λ approaching 1, the terms Φ_p, E, and Ψ_D tend to 1, $\frac{\pi}{2}$, and 2, respectively, and u_∞ is given by the Stokes' law, $u_\infty=\frac{D_p^2\rho_p g}{18\mu}$, for $Re<0.1$.

[13] The value of the settling speed is deduced from (11) by solving numerically, for a given equivalent diameter (D_p) and aspect ratio (λ), first the elliptic integral and then the nonlinear equation using the bisection method by bracketing u_∞ values between 0 and 1 m s^{-1}. Figure 1 shows the results of the calculation with D_p varying from 0.1 to 100 μm, and λ from 1 to 10 with a step of 1. The settling speed and the relative difference between spherical and non-spherical ($\Delta u_\infty=100\times\frac{\mu_\infty(\lambda=1)-u_\infty(\lambda)}{u_\infty(\lambda=1)}$) are given on the left and right panels, respectively. For spherical particles, the settling speed varies quasi-linearly with the square of the particle size for $D_p<10$ μm. Beyond that diameter the settling speed is less sensitive to the particle size and ultimately will vary as the square root of the particle diameter as the drag C_D tends to a constant value of 0.44. For all particle sizes, as the aspect ratio increases from 2 to 10, the settling speed decreases. For $D_p=1$ μm particle, the reduction is around 2%, 30%, and 55% for aspect ratio 2, 5, and 10, respectively. These values are comparable to the values calculated by *Fuchs* [1964]: 5%, 20%, and 60% respectively. The decrease of settling speed goes through an extremum for $D_p=60$ μm. The maximum reduction of speed is 85% for $\lambda=10$ which could be translated into a doubling of particle lifetime with respect to gravitational settling. *Fuchs* [1964] did not calculate the settling speed reduction for $Re>0.1$.

[14] Using the frequency distribution of the aspect ration λ given by *Okada et al.* [2001] and assuming that it is invariant of the particle size, the settling speed is calculated by solving (11). Figure 2 shows the percentage of relative reduction Δu_∞ resulting from the calculation. The maximum reduction is only 10% for particle diameter around 60 μm. Surprisingly, for particles less than 1 μm diameter there is a negative reduction or an increase of the settling speed. Although this increase is less than 2%, it is interesting to understand its origin. In (11), the terms E and Φ_p decrease with increasing D_p while Ψ_D varies in the other direction. For $\lambda<2$, the term $E\times\Psi_D$ is lower than 1. *Fuchs* [1964] observed also an increase of settling speed for particles settling along their polar axis and for aspect ratio less than 4. Figure 3 shows the values of Δu_∞ for λ varying from 0.2 to 2 with a 0.2 increment. For aspect ratio λ less than 2, the reduction Δu_∞ crosses the x axis at a diameter D_p which decreases from 60 with $\lambda=1.1$ to 0.1 for $\lambda=1.9$.

[15] The relative reduction of the settling speed Δu_∞ has been fitted to a Gaussian and quadratic function using six parameters a_i,

$$\Delta u_\infty \sim a_0\exp\left(\frac{-z^2}{2}\right)+a_3+a_4x+a_5x^2 \tag{12}$$

with $z=\frac{x-a_1}{a_2}$ and $x=\log_{10}D_p$. The values of a_i for different equivalent diameter D_p are given in Table 2. The fitted values are slightly overestimated for $D_p\sim0.1$ which is not problematic because particles with such small diameter are

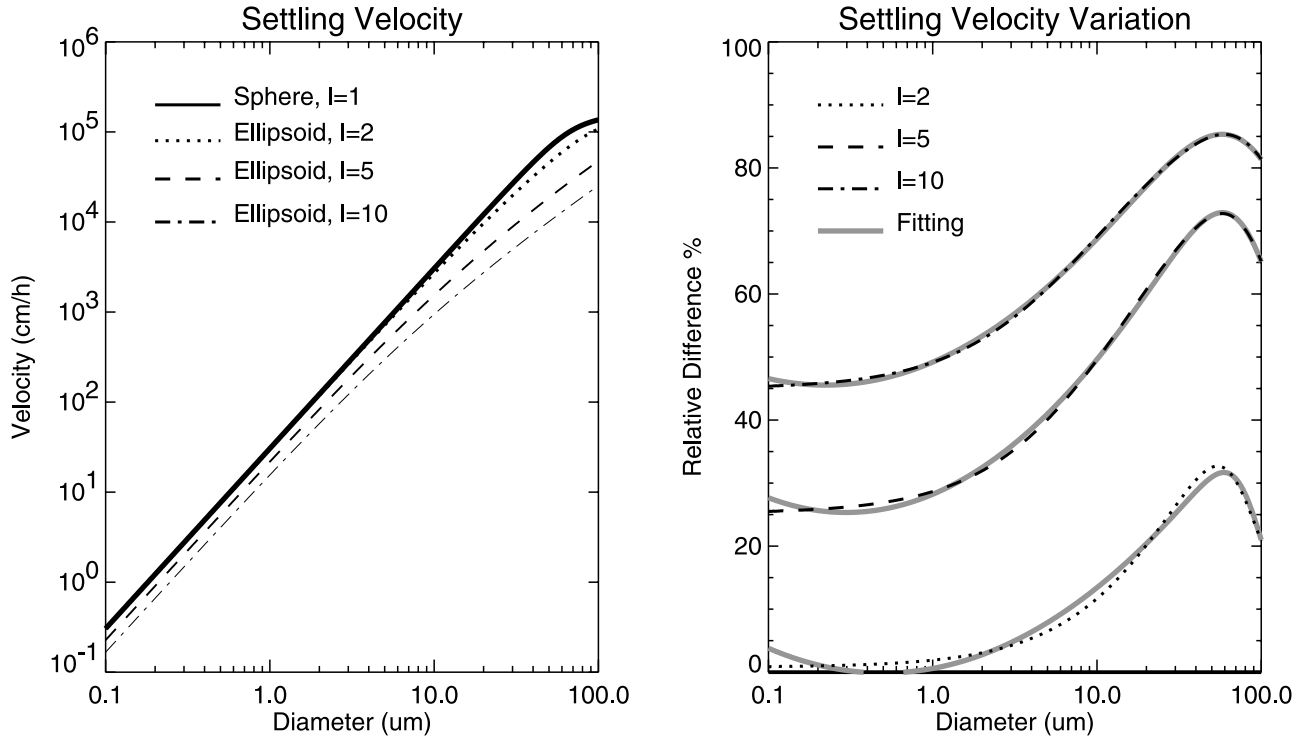

Figure 1. Fall speed of ellipsoid particles (left panel) and the relative reduction (%) of calculated settling speed (right panel) with size ranging from 0.1 to 100 μm and aspect ratio varying from 2 to 10 with an increment of 1. The black lines are calculated values from the momentum equation (11), and the gray lines are fitted values. The dotted line is for $\lambda = 2$, the dashed line is for $\lambda = 5$, and the dash-dotted line is for $\lambda = 10$.

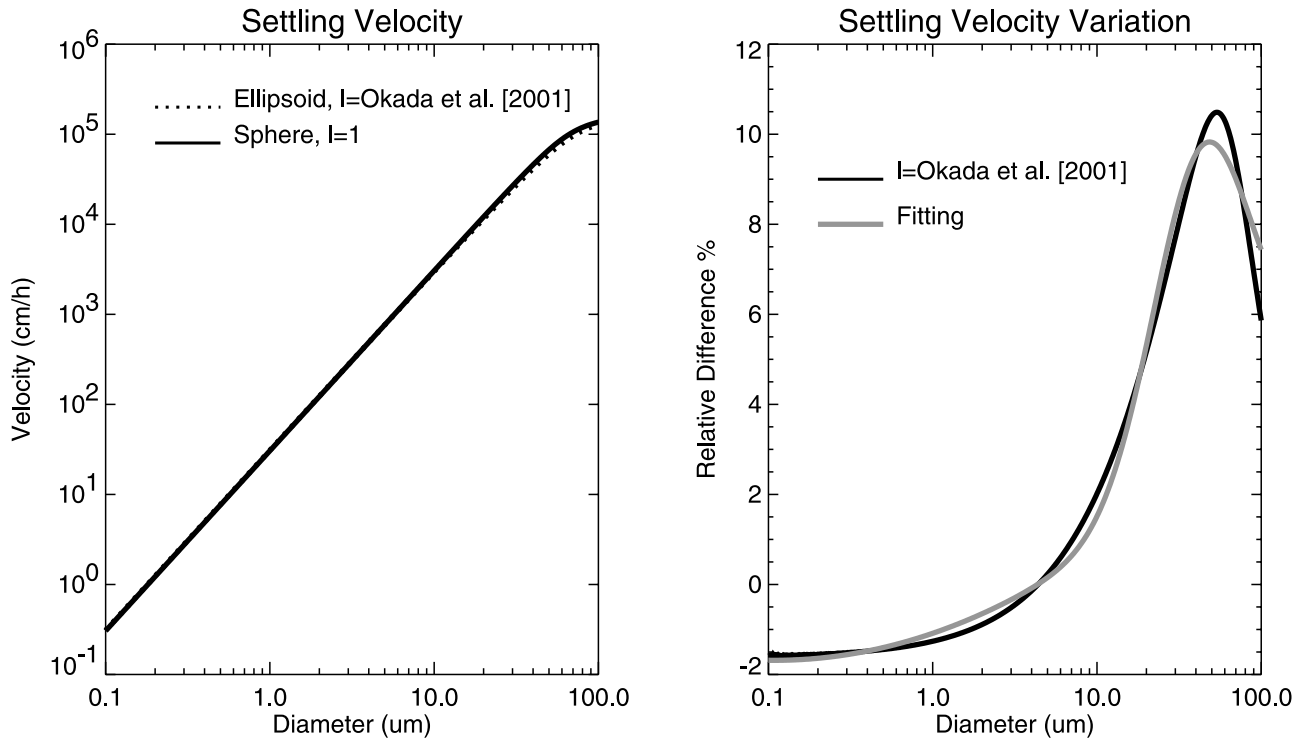

Figure 2. Relative reduction of settling speed of particles with the *Okada et al.* [2001] shape distribution.

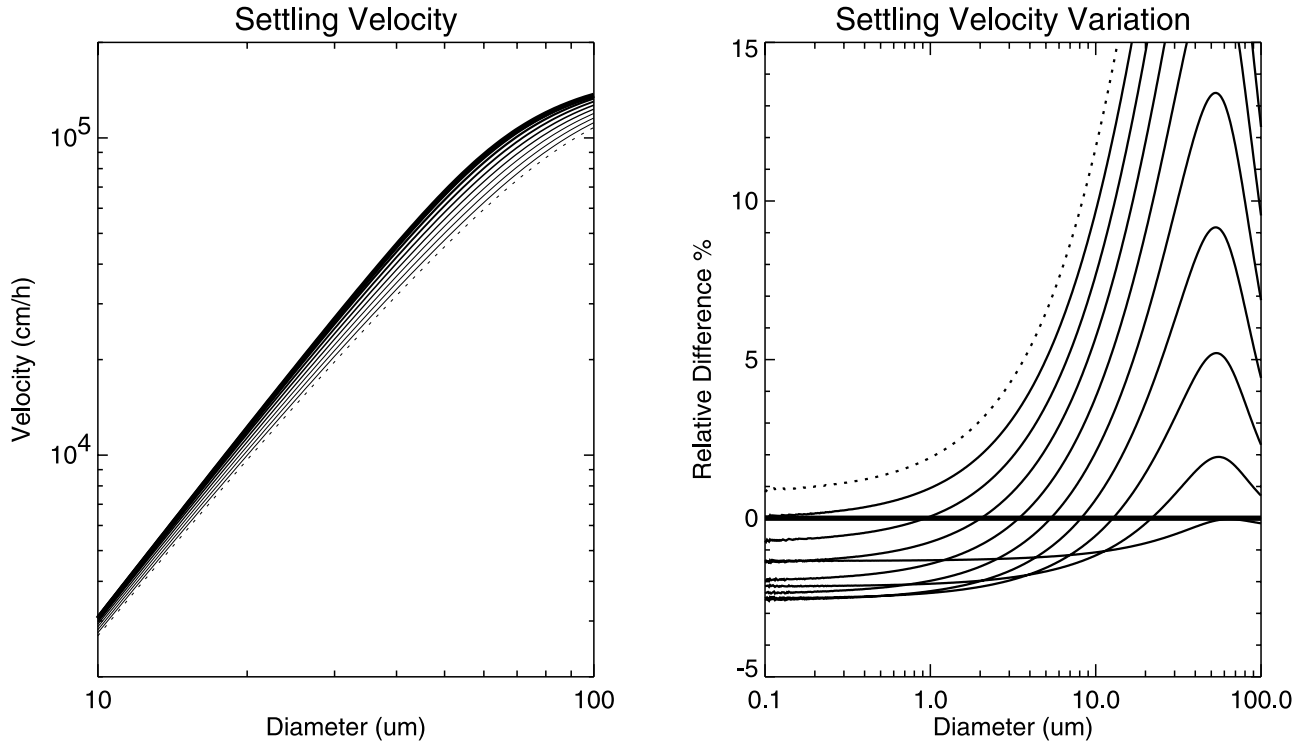

Figure 3. Relative reduction (%) of calculated settling speed with size ranging from 0.1 to 100 μm and aspect ratio varying from 1.1 to 2 with an increment of 0.1. The dotted line is for $\lambda = 2$.

primarily removed by precipitation and not by gravitational settling, as shown in the next section.

4. Simulation of Nonspherical Dust Particles With Global Ozone Chemistry Aerosol Radiation and Transport (GOCART)

[16] To investigate the effect of nonsphericity on dust distribution, the Georgia Institute of Technology Goddard GOCART model is used. The GOCART model has been described in details elsewhere [*Chin et al.*, 2000; *Ginoux et al.*, 2001; *Chin et al.*, 2002]. The model simulates the global distribution of dust, sulfate, carbonaceous, and sea-salt aerosols using assimilated meteorological fields by the Goddard Earth Observing System Data Assimilation System (GEOS DAS). The GEOS DAS fields are used to drive the dust emission, advection, convection, diffusion, removal by gravitational settling, dry deposition at the surface, and wet deposition. The wet deposition in the model includes rainout (in-cloud precipitation) and washout (below cloud precipitation) in large-scale precipitation and in deep convective cloud updraft. These last two fields are provided by GEOS DAS. *Ginoux et al.* [2001] have shown that with GOCART model, the main removal process is dry deposition: gravitational settling for large particles and impaction at the surface for submicron particles. Because the dust sources are located in arid regions, wet deposition is a significant removal mechanism only for submicron particles. Globally the wet deposition accounts for only 10–15% of the total dust removal. The dust sources are specified using a source function derived from the study of *Prospero et al.* [2002]. The dust emission is modified from the study of *Ginoux et al.* [2001]: the threshold velocity is here parameterized following the study of *Iversen and White* [1989]. Another difference with the study of *Ginoux et al.* [2001] is the addition of 4 size bins extending the size range up to 80 μm. The 0.2–80 μm size range is divided into for 8 size bins with their properties given in Table 3. The mass size distribution into each classes is assumed constant except for the submicron particles for which it is assumed a lognormal distribution with a median diameter of 1.5 μm and a geometric standard deviation of 2. A 6 week simulation is performed from 1 March to 15 April 2001. The first 4 weeks are used for model spin-up.

4.1. Gravitational Settling Schemes

[17] Two numerical schemes are used to solve the advective transport by gravitational settling. The first one is the

Table 2. Values of the Six Parameters Fitting the Function $f(x) = a_0\exp\left(-\frac{z^2}{2}\right) + a_3 + a_4x + a_5x^2$ with $z = \frac{x-a_1}{a_2}$ and $x = \log_{10}D_p$, and D_p is the Diameter in Units of μm for Nine Values of the Aspect Ratio λ

λ	a_0	a_1	a_2	a_3	a_4	a_5
2	−36.234	2.186	0.180	0.598	4.808	8.011
3	−55.657	2.265	0.221	11.234	8.512	10.602
4	−66.572	2.361	0.270	20.719	10.218	10.766
5	−77.18	2.472	0.324	28.232	10.978	10.426
6	−88.068	2.586	0.376	34.193	11.292	9.994
7	−99.492	2.701	0.426	39.013	11.384	9.577
8	−110.926	2.813	0.472	42.992	11.362	9.200
9	−121.087	2.915	0.513	46.338	11.280	8.856
10	−130.914	3.012	0.552	49.196	11.167	8.551

Table 3. Physical Properties of the Size Bins

Bin	Size Range (μm)	Size Distribution	Source Fraction	D_p (μm)	ρ_p (kg m^{-1})	Reduction of u_∞		
						$\lambda = 1$	$\lambda = 2$	$\lambda = 5$
1	0.2–2	$\frac{dm}{d\ln r} = \text{cst}$	0.1	1.5	2600	1	0.9831	0.6951
2	2–4	$\frac{dm}{dr} = \text{cst}$	0.25	3	2600	1	0.9528	0.6416
3	4–6	$\frac{dm}{dr} = \text{cst}$	0.25	5	2600	1	0.9213	0.59
4	6–12	$\frac{dm}{dr} = \text{cst}$	0.25	9	2600	1	0.8853	0.5335
5	12–20	$\frac{dm}{dr} = \text{cst}$	0.25	16	2600	1	0.82	0.4347
6	20–30	$\frac{dm}{dr} = \text{cst}$	0.25	25	2600	1	0.7751	0.37
7	30–50	$\frac{dm}{dr} = \text{cst}$	0.25	40	2600	1	0.7133	0.2953
8	50–70	$\frac{dm}{dr} = \text{cst}$	0.25	60	2600	1	0.6831	0.2711

upwind scheme, used by *Ginoux et al.* [2001], and is given by the algebraic form:

$$(m_p)_j^{n+1} = (m_p)_j^n + \frac{u_\infty \Delta t}{\Delta z}\left[(m_p)_{j-1}^n - (m_p)_j^n\right] \tag{13}$$

where $(m_p)_j^n$ is the dust mass at grid level j and time n, Δt is the time step and Δz is the vertical grid spacing. The scheme is conservative and computationally efficient, but it is diffusive. The second scheme, developed by *Prather* [1986], is accurate and nondiffusive and it preserves the tracer structures by conserving the second-order moments of the spatial distribution. The drawback of the method is that it requires transport of the moments, which is computationally expensive. Both schemes are Eulerian and necessitate to satisfy the Courant-Friedricks-Levy (CFL) condition:

$$\Delta t < \frac{\Delta z}{u_\infty} \tag{14}$$

For all simulations, the time step is imposed to respect the CFL condition. The GOCART model time step is set to 20 min. At every model time step, the minimum Δz at every grid point is calculated, and a subtime step is imposed for each particle sizes such that its value is half $\frac{\Delta z_{minimum}}{u_\infty}$.

5. Effect of Nonsphericity on Model Results

[18] In this section, the effects of nonsphericity on simulated dust mass column, size distribution and surface concentration are analyzed, and the benefits of implementing nonsphericity in transport models are discussed.

5.1. Effect of Nonsphericity on Dust Mass Column

[19] Figure 4 shows the global distribution of dust mass column for spherical particles using the *Prather* [1986] scheme (upper panel), the difference of mass column when using the upwind scheme (second panel), the difference of mass column between spherical and ellipsoid with $\lambda = 2$ (third panel) and 5 (fourth panel). The distributions are temporal average over the first 2 weeks of April 2001. The distribution of the upper panel is typical of Spring, with maxima dust loading over Sahel (Bodele depression) and China (Taklamakan and Gobi deserts). The transport from Africa to the Atlantic and from China to the North Pacific is clearly apparent. The second panel shows that diffusive numerical treatment of the settling underestimates the mass loading by as much as factor 2. *Schulz et al.* [1999] have already indicated the need for higher-order numerical technique for treating sedimentation process; but Figure 4 shows that the effect of nonsphericity is of second order compare to numerical diffusion. From the two bottom

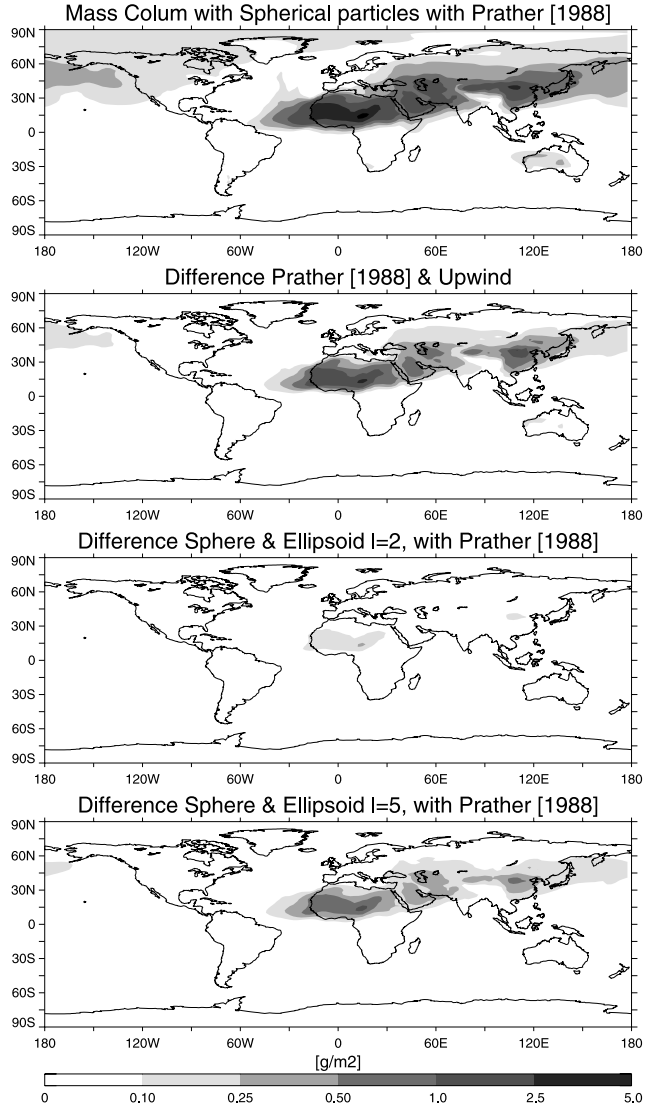

Figure 4. Simulated mass column (g m^{-2}) considering spherical particles using the *Prather* [1986] advective scheme (top), absolute difference with upwind scheme (second panel), and with *Prather* [1986] scheme and prolate ellipsoid when $\lambda = 2$ (third panel) and 5 (bottom).

Table 4. Global Dust Load Change and Lifetime

	Load Change (%)			Life (days)		
Size (μm)	λ = 1	λ = 2	λ = 5	λ = 1	λ = 2	λ = 5
0.2–2	13.07	13.07	13.13	13	13	13
2–4	26.5	26.63	27.2	13	13	13
4–6	26.91	27.34	29.22	11	12	13
6–12	20	21.09	25.47	7	8	10
12–20	10.19	11.84	17.63	2.5	4	6
20–30	2.91	4.15	10.05	1	1.5	3.5
30–50	0.35	0.54	1.83	0.1	0.2	0.6
50–70	0.01	0.09	0.41	0.01	0.03	0.14
0.2–70	100	104.74	125.96	5	5.2	6.3

panels, it appears that nonsphericity affects the dust mass column only for very elongated particles. The effect is negligible with λ = 2. For λ = 5, the effect is significant mainly in the source area, but it also amplifies the long-range transport as it can be seen over the North Atlantic and Pacific. Table 4 gives the percentage difference of dust load, relative to the total dust loading of spherical particles, and the lifetime, for the 8 size bins and 3 aspect ratios. The values are established from the simulations of the first 2 weeks of April using the *Prather* [1986] scheme. It is important to note that the values in Table 4 are representative of April 2001, which is characterized by two severe dust storms over China (so-called perfect dust storms). Therefore, the lifetimes are not necessarily representative of other periods. The Asian dust storms are characterized by high altitude transport [*Ginoux et al.*, 2001] and the results of this study will eventually overestimate the more general effects of nonsphericity. For any shape factor, Table 4 indicates that the maximum dust loading is around 4–6 μm. As the size of the particle increases, the dust load is more sensitive to the shape factor, but the relative contribution rapidly declines. The lifetime of the largest particles with λ = 5 is a factor 10 higher than the equivalent spherical particles, but it is still a factor 100 lower than for particles lower than 12 μm. The effect on the global dust loading, for λ = 5, is an increase of the order of 25% which is not negligible.

5.2. Effect of Nonsphericity on Size Distribution

[20] Figure 5 shows the comparison between simulated and measured volume size distribution at six sites, in North Africa, and East Asia. The measured values have been retrieved from the AERONET data by an iterative inversion algorithm [*Dubovik and King*, 2000]. This algorithm does not take into account nonsphericity. The size distributions are average values of the screened data using the criteria described by *Dubovik et al.* [2000]. The simulated values correspond to the exact same day and time (±3 hours) the data were collected. The six simulated size distributions include the *Prather* [1986] and the upwind schemes with λ = 1, 2, and 5. With the *Prather* [1986] scheme, the simulated size distribution of spherical particle fit considerably better the observations. The comparison between the two settling schemes clearly shows that without a proper scheme wrong conclusions on the nonsphericity could be established based on numerical errors. *Dubovik et al.* [2000] have indicated that the error in the retrieval algorithm is lower than 10–35% for dust particles in the range 0.1 < radius < 7, but is as high as 80–100% for larger particles. In Figure 5, a 35% error for particles less than 7 μm and a 100% error for larger particles are shown. None of the simulated size distributions are within the observation errors for all radii and at every

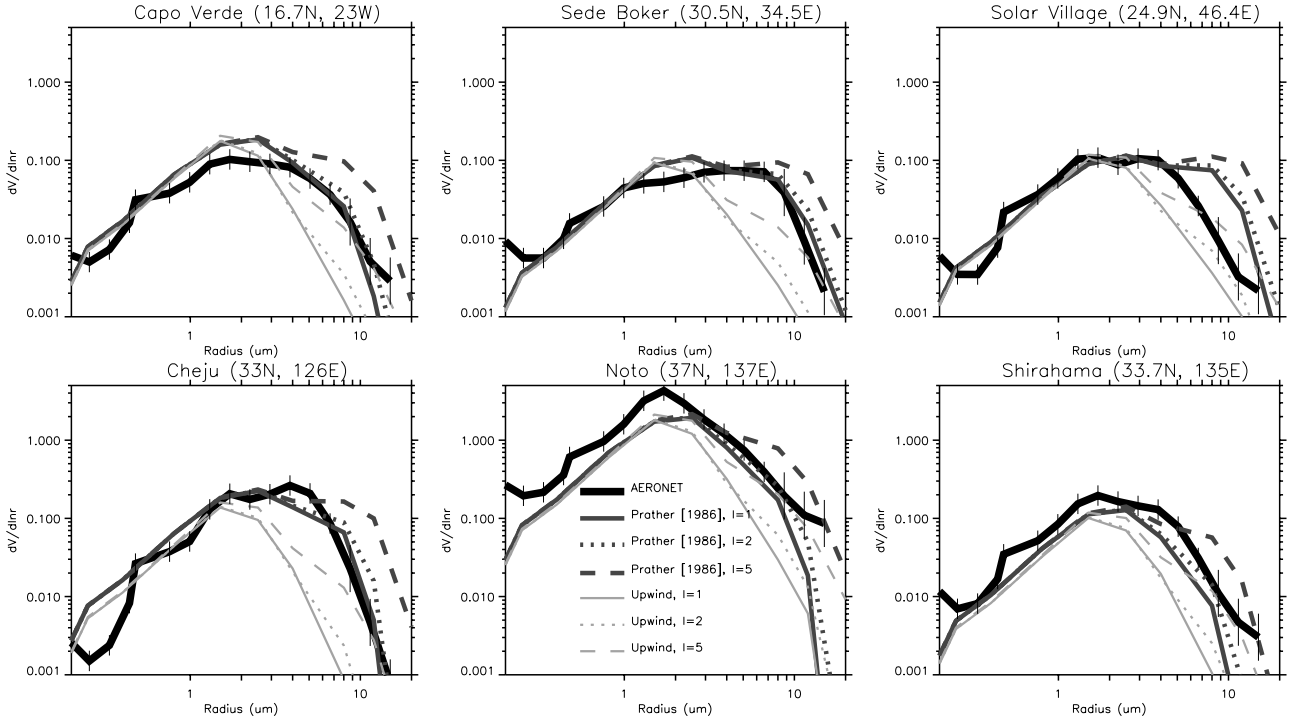

Figure 5. Comparison between observed (black bold line) with error bars (vertical thin lines) and simulated volume size distribution ($\mu m^3\ \mu m^{-2}$) with upwind scheme and λ = 1 (light gray), 2 (dots light gray), and 5 (dash light gray) and with the *Prather* [1986] scheme and λ =1 (dark gray), 2 (dots dark gray), and 5 (dash dark gray).

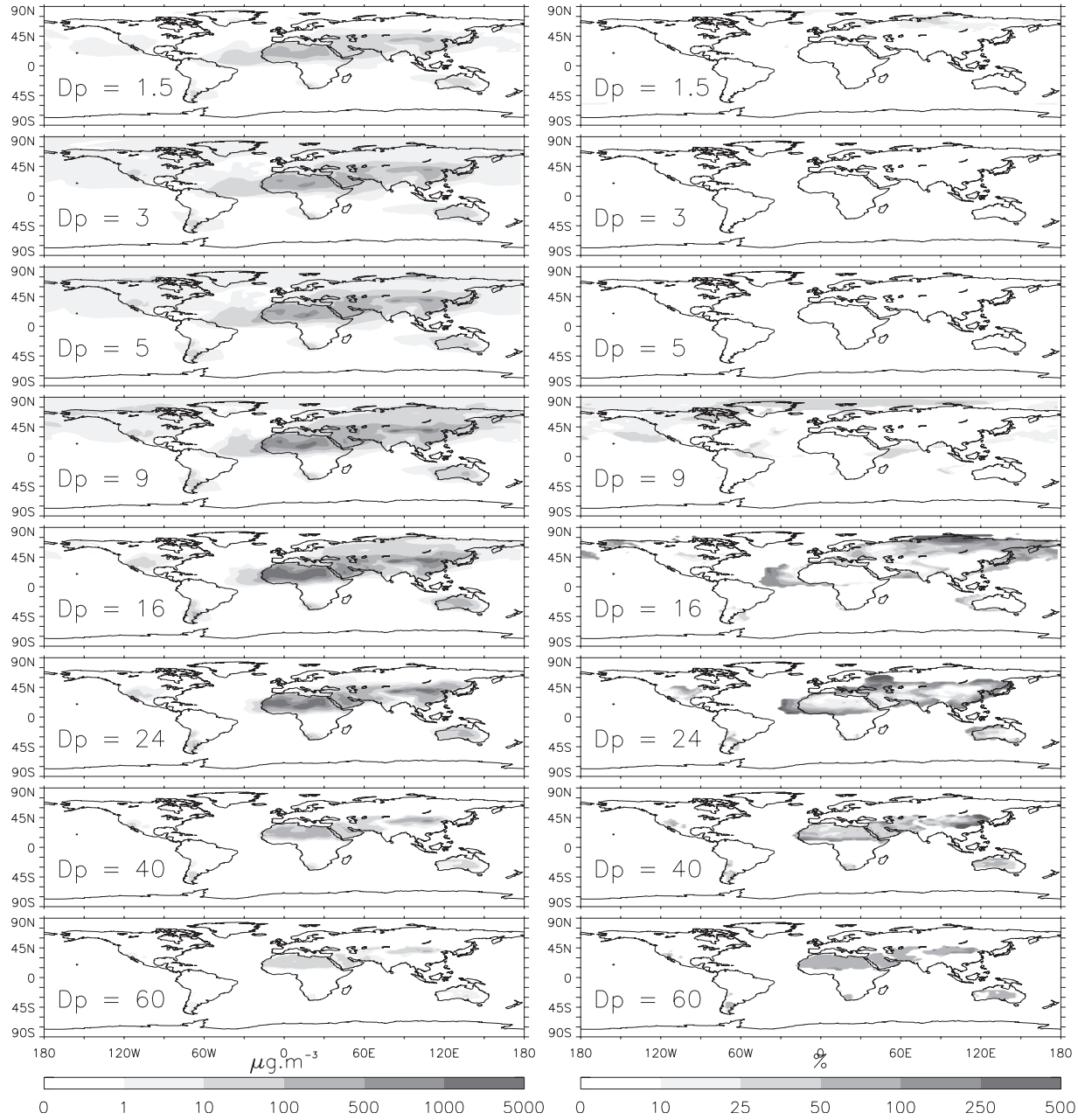

Figure 6. Simulated surface concentration ($\mu g\ m^{-3}$) of spherical particles and relative difference of concentration (%) with ellipsoid $\lambda = 2$ for 8 diameter of particles.

stations. The discrepancy is quite low for spherical and ellipsoid ($\lambda = 2$) with the *Prather* [1986] scheme but there is no clear improvement with a particular assumption regarding the shape of the particles. The size distributions with an aspect ratio of 5 tend to produce a secondary maximum around 8 μm radius. However, an aspect ratio of 5 systematically overestimates the size distribution and if there are such elongated particles, their frequency should be rather low.

5.3. Effect of Nonsphericity on Surface Concentration

[21] As the lifetime of particles increases with λ, an increase of surface concentration should be expected. Such increase will vary spatially depending of the other transport and removal processes. The interesting aspect to know is the eventual existence of a systematic underestimation of simulated surface concentration when comparing with in situ measurements, and if this bias is depending of the location. Figure 6 shows the surface concentration of nonspherical particle with $\lambda = 2$, and the percentage difference with respect to spherical particles, for the 8 size bins. The concentrations are average values over the first 2 weeks of April 2001 using the *Prather* [1986] scheme. The concentrations of particles smaller than 6 μm are unaffected by the nonsphericity, as it is expected for particles primarily removed by wet deposition. For particles between 6 and 20 μm, the nonsphericity has a significant impact on surface concentration. The percentage change increases from ~20% to 200% has D_p increases from 9 to 15 μm, but the spatial range decreases. For particle larger than 20 μm, the impact

is purely local over the source area and the percentage change of surface concentration tends toward the value of reduction of settling speed given in Table 3. The contribution to total dust concentration is predominantly attributed to particles less than 12 μm outside source area. In that size range, the difference of surface concentration is less than 10% everywhere. Over the source area, particles around 16 μm dominate the total mass concentration but there is no impact of nonsphericity in such regions. For larger particles, the nonsphericity change by about 50% the total concentration, but their contribution to the mass concentration is very low. The only regions where nonsphericity seems to play a significant role, of the order of 10–20%, is outside but in the vicinity of the source regions. The two typical regions are the Eastern part of the North Atlantic, and the sea of Japan, off the coast of China. In summary, global modelers will not significantly improve their results by including nonsphericity in the treatment of sedimentation. However, including nonspherical effects actually reduces the computational cost because a reduction of u_∞ relaxes the CFL condition. The only added cost is to multiply the settling speed by the corresponding reduction values given in Table 3. The benefit to regional model is more appreciable, particularly for the study of dust export from source areas (i.e., Ace-Asia field campaign). If one can measure the shape of particle larger than 4 μm to complement the *Okada et al.* [2001] data, the model simulations could be improved by about 10–20% in case of nonspherical particles with $\lambda = 2$.

6. Conclusions

[22] The effects of nonsphericity on dust mass column, size distribution and surface concentration is investigated at the global scale. These effects are analyzed using the global transport model GOCART with a modified settling scheme. The settling speed in this scheme is derived from a nonlinear equation assuming that the particle's shape corresponds to prolate ellipsoid and the particles are randomly oriented in their settling. The choice of the particle shape is based on in situ measurements of Asian dust showing that particles shape look like ellipsoid with the most frequent aspect ratio around 1.5. Higher aspect ratios are observed, although are less frequent. The analysis is performed for prolate ellipsoid with aspect ratios varying from 1 (spherical particles) to 10 (very elongated particle). The settling speed is reduced for all particle sizes when the aspect ratio is greater than 1.5. The reduction is maximum for particle size around 60 μm where it varies from 10% ($\lambda = 2$) to 85% ($\lambda = 10$). For lower λ, the sign of the reduction is a function of the particle size and the λ value. The reduction is approximated by a quadratic and a Gaussian with 6 parameters. The fitting parameters for $\lambda = 2$ and 5 are implemented in the GOCART global transport model. The size distribution is discretized into eight size bins, ranging from 0.2 to 70 μm, and a simulation covering the first 2 weeks of April 2001 is realized. The results indicate no significant effect on dust loading for $\lambda = 2$ and a 25% increase for $\lambda = 5$. Comparison of size distribution with ground-based measurements indicate that particles with aspect ratio of 5 should be rather infrequent. The major effect with such aspect ratio is to produce a secondary maximum around 8 μm radius. For lower aspect ratios, the model imprecision does not allow to determine the effect of nonsphericity on the size distribution. The comparison of two numerical techniques for solving sedimentation shows that the effect of nonsphericity is of second order compare to numerical diffusion. The use of a higher-order method considerably improves the comparison with observed size distribution, particularly for the largest particles. This suggests that models which have difficulties to reproduce the concentration of particles with diameter larger than 10 μm should try a higher-order advective scheme. The effect on surface concentration is more complex and varies spatially with the particle size. The most affected particles are in the 6–15 μm size range outside the source regions and particles larger than 20 μm over the source area. The contribution to the total dust concentration is rather limited and does not exceed 20% a short distance from the source regions. Global modeling results will not significantly improve from the implementation of nonsphericity. On the other hand, its implementation will relax the CFL conditions which is a major burden when solving advective equation. The benefit for regional study of dust export from source area could be more substantial but there is unfortunately no existing data on shape factor for particles greater than 4 μm. The choice of a shape factor should then be conservative and value of 2 or less should be selected. Based on existing data, it does not seem that the nonsphericity of particles could explain the observed long-range transport of so-called giant particles. However, if observation of their shape reveals aspect ratios greater than 2, then these conclusions should be revised.

[23] **Acknowledgments.** I am very grateful to an anonymous reviewer and to Michel Riethmuller (Von Karman Institute, Belgium) to inform me about different studies on nonsphericity. I wish to thank Michael Prather (University of California, Irvine) for giving me his advective scheme. I am also very grateful to Brent Holben (AERONET, NASA GSFC, USA) for giving me access to the Sun photometer data at Cheju, Sede Boker, Shirahama, and Solar Village, to Didier Tanre (PHOTON, Universit de Lille, France) for the Sun photometer data at Cape Verde, and to Itaru Sano for the Sun photometer data at Noto. I would like to thank Oleg Dubovik and Alexander Smirnov for their help in using properly the AERONET data. This work is supported by a NASA grant NAG-35-694.

References

Boothroyd, R. G., *Flow Gas–Solids Suspensions*, 289 pp., Chapman Hall, New York, 1971.

Caquineau, S., A. Gaudichet, L. Gomes, M.-C. Magonthier, and B. Chatenet, Saharan dust: Clay ratio as a relevant tracer to assess the origin of soil-derived aerosols, *Geophys. Res. Lett.*, *25*, 983–986, 1998.

Chin, M., R. B. Rood, S.-J. Lin, J.-F. Muller, and A. M. Thompson, Atmospheric sulfur cycle simulated in the global model GOCART: Model description and global properties, *J. Geophys. Res.*, *105*, 24,671–24,687, 2000.

Chin, M., P. Ginoux, S. Kinne, O. Torres, B. N. Holben, B. N. Duncan, R. V. Martin, J. A. Logan, A. Higurashi, and T. Nakajima, Tropospheric aerosol optical thickness from the GOCART model and comparisons with satellite and Sun photometer measurements, *J. Atmos. Sci.*, *59*, 461–483, 2002.

Colarco, P. R., O. B. Toon, O. Torres, and P. Rasch, Determining the UV imaginery index of refraction of Saharan dust particles from Total Ozone Mapping Spectrometer data using a three-dimension model of dust transport, *J. Geophys. Res.*, *107*(D16), 4289, doi:10.1029/2001JD000903, 2002.

Dubovik, O., and M. D. King, A flexible inversion algorithm for retrieval of aerosol optical properties from Sun and sky radiance measurements, *J. Geophys. Res.*, *105*, 260,673–260,696, 2000.

Dubovik, O., A. Smirnov, B. N. Holben, M. D. King, Y. J. Kaufman, T. F. Eck, and I. Slutsker, Accuracy assessments of aerosol optical properties retrieved from AERONET Sun and sky-radiance measurements, *J. Geophys. Res.*, *105*, 9791–9806, 2000.

Fuchs, N. A., *The Mechanics of Aerosols*, Pergamon, New York, 1964.
Ginoux, P., M. Chin, I. Tegen, J. M. Prospero, B. Holben, O. Dubovik, and S.-J. Lin, Sources and distributions of dust aerosols simulated with the GOCART model, *J. Geophys. Res.*, *106*, 20,255–20,273, 2001.
Glaccum, R. A., and J. M. Prospero, Saharan aerosols over the tropical North Atlantic: Mineralogy, *Mar. Geol.*, *37*, 295–321, 1980.
Goudie, A. S., and N. J. Middleton, Saharan dust storms: Nature and consequences, *Earth Sci. Rev.*, *56*, 179–204, 2001.
Grim, R. E., *Clay Mineralogy*, 596 pp., McGraw-Hill, New York, 1968.
Iversen, J. D., and B. R. White, Saltation threshold on Earth Mars and Venus, *Sedimentology*, *36*, 253–271, 1989.
Kagermann, H., and W. E. Khler, On the motion of nonspherical particles in a turbulent flow, *Physica*, *116A*, 178–205, 1982.
Kalashnikova, O. V., and I. N. Sokolik, Importance of shapes and compositions of wind-blown dust particles for remote sensing at solar wavelengths, *Geophys. Res. Lett.*, *29*, doi:10.1029/2002GL014947, 2002.
Koepke, P., and M. Hess, Scattering functions of tropospheric aerosols: The effect of non-spherical particles, *Appl. Opt.*, *27*, 2422–2430, 1988.
Krotkov, N. A., D. E. Flittner, A. J. Krueger, A. Kostinski, C. Riley, W. Rose, and O. Torres, Effect of particle non-sphericity on satellite monitoring of drifting volcanic ash clouds, *J. Quant. Spectrosc. Radiat. Transfer*, *63*, 613–630, 1999.
Mischenko, M. I., Light scattering by randomly oriented axially symmetric particles, *J. Opt. Soc. Am.*, *8*, 871–882, 1991.
Mischenko, M. I., and L. D. Travis, Light scattering by polydispersions of randomly oriented spheroids with sizes comparable to wavelength of i observations, *Appl. Opt.*, *33*, 7206–7225, 1994.
Mischenko, M. I., A. A. Lacis, B. E. Carlson, and L. D. Travis, Non-sphericity of dust like tropospheric aerosols: Implications for aerosol remote sensing and climate modeling, *Geophys. Res. Lett.*, *22*, 1077–1080, 1995.
Okada, K., J. Heintzenberg, K. Kai, and Y. Qin, Shape of atmospheric mineral particles collected in three Chinese arid-regions, *Geophys. Res. Lett.*, *28*, 3123–3126, 2001.
Prather, M. J., Numerical advection by conservation of second-order moments, *J. Geophys. Res.*, *91*, 6671–6681, 1986.
Prospero, J. M., P. Ginoux, O. Torres, S. Nicholson, and T. Gill, Environmental characterization of global sources of atmospheric soil dust identified with the NIMBUS-7 TOMS Absorbing Aerosol Product, *Rev. Geophys.*, *40*(1), 1002, doi:10.1029/2000RG000095, 2002.
Schulz, F. M., K. Stammes, and J. J. Stammes, Shape dependence on the optical properties in size-shape distributions of randomly oriented prolate spheroids, including highly elongated shapes, *J. Geophys. Res.*, *104*, 9413–9421, 1999.
Seinfeld, J. and S. N. Pandis, *Atmospheric Chemistry and Physics*, 1326 pp., John Wiley, New York, 1998.
Sokolik, N., and O. B. Toon, Direct radiative forcing by anthropogenic mineral aerosols, *Nature*, *381*, 681–683, 1996.
Tegen, I., and I. Fung, Modeling of mineral dust in the atmosphere: Sources, transport, and optical thickness, *J. Geophys. Res.*, *99*, 22,897–22,914, 1994.
Tegen, I., A. Lacis, and I. Fung, The influence of mineral aerosol from disturbed soils on the global radiation budget, *Nature*, *380*, 419–422, 1996.
Toon, O. B., et al., *Icarus*, *43*, 260–282, 1980.
Turco, R. P., O. B. Toon, R. C. Whitten, R. G. Keesee, and D. Hollenbach, Noctilucent clouds: Simulation studies of their genesis, properties and global influences, *Planet. Space Sci.*, *30*, 1147–1181, 1982.
Weaver, C. J., P. Ginoux, N. C. Hsu, M.-D. Chou, and J. Joiner, Radiative forcing of Saharan dust: GOCART model simulations compared with ERBE data, *J. Atmos. Sci.*, *59*, 736–747, 2002.

P. Ginoux, National Aeronautics and Space Administration (NASA) Goddard Space Flight Center, Code 916, Greenbelt, MD 20771, USA. (ginoux@rondo.gsfc.nasa.gov)